PNAS RESEARCH ARTICLE | EARTH, ATMOSPHERIC, AND PLANETARY SCIENCES

Long- and short-term coupling of sea surface temperature and atmospheric CO_2 during the late Paleocene and early Eocene

Dustin T. Harper[a,1], Bärbel Hönisch[b], Gabriel J. Bowen[a], Richard E. Zeebe[c], Laura L. Haynes[d], Donald E. Penman[e], and James C. Zachos[f]

Affiliations are included on p. 7.

Edited by John Valley, University of Wisconsin-Madison, Madison, WI; received October 26, 2023; accepted June 4, 2024

The late Paleocene and early Eocene (LPEE) are characterized by long-term (million years, Myr) global warming and by transient, abrupt (kiloyears, kyr) warming events, termed hyperthermals. Although both have been attributed to greenhouse (CO_2) forcing, the longer-term trend in climate was likely influenced by additional forcing factors (i.e., tectonics) and the extent to which warming was driven by atmospheric CO_2 remains unclear. Here, we use a suite of new and existing observations from planktic foraminifera collected at Pacific Ocean Drilling Program Sites 1209 and 1210 and inversion of a multiproxy Bayesian hierarchical model to quantify sea surface temperature (SST) and atmospheric CO_2 over a 6-Myr interval. Our reconstructions span the initiation of long-term LPEE warming (~58 Ma), and the two largest Paleogene hyperthermals, the Paleocene–Eocene Thermal Maximum (PETM, ~56 Ma) and Eocene Thermal Maximum 2 (ETM-2, ~54 Ma). Our results show strong coupling between CO_2 and temperature over the long- (LPEE) and short-term (PETM and ETM-2) but differing Pacific climate sensitivities over the two timescales. Combined CO_2 and carbon isotope trends imply the carbon source driving CO_2 increase was likely methanogenic, organic, or mixed for the PETM and organic for ETM-2, whereas a source with higher $\delta^{13}C$ values (e.g., volcanic degassing) is associated with the long-term LPEE. Reconstructed emissions for the PETM (5,800 Gt C) and ETM-2 (3,800 Gt C) are comparable in mass to future emission scenarios, reinforcing the value of these events as analogs of anthropogenic change.

carbon dioxide | climate sensitivity | Paleocene–Eocene | boron proxies | Paleocene–Eocene Thermal Maximum

Since the Cambrian explosion of metazoan life nearly 540 million years ago, Earth has experienced many episodes of long- and short-term warming generally associated with and attributed to rising greenhouse gas (GHG) levels (1). A particularly prominent and enigmatic period of long-term warming occurred during the fairly recent transition from the late Paleocene to the early Eocene (LPEE), when global temperatures increased by 4 to 5 °C over a ~6-million year (Myr) period (~59 to 53 Ma). High-resolution, orbitally tuned benthic foraminiferal isotope records from Atlantic and Pacific basins (ODP Sites 1262 and 1209) show that the long-term trend in climate during the LPEE initiated relatively abruptly, with a stepwise transition (decrease in $\delta^{18}O$ values indicative of ~2 °C of warming, and a +1‰ increase in $\delta^{13}C$ values) during the peak of the Paleocene Carbon Isotope Maximum (PCIM; peak ca. 58 Ma; Fig. 1 and *SI Appendix*, Fig. S1). Long-term LPEE warming climaxed during the Early Eocene Climatic Optimum (EECO; 53 to 50 Ma), the warmest interval of the Cenozoic (2–4), and was associated with elevated atmospheric CO_2 (5). Throughout the LPEE, repeated abrupt global warming events called hyperthermals occurred, including the Paleocene–Eocene Thermal Maximum (PETM) and Eocene Thermal Maximum 2 (ETM-2).

LPEE warming appears to have been associated with rising atmospheric CO_2 as constrained by various proxies, though the extent of the coupling is unclear, in part due to the low resolution and high uncertainty in proxy data (16, 17). The LPEE climate signal is strongly coupled with carbon system parameters in addition to atmospheric CO_2, specifically decreases in ocean stable carbon isotope ($\delta^{13}C$) composition (18) and increases in carbonate ion saturation as inferred from the deepening carbonate compensation depth (CCD) (19, 20). This was likely driven by enhanced terrestrial carbonate and silicate rock weathering due to elevated atmospheric CO_2 and temperature. Hyperthermals are similarly associated with perturbations to the carbon cycle and are in part characterized by abrupt decreases in ocean $\delta^{13}C$ values, elevated CO_2, and an initial shallowing of the CCD as expected for abrupt events associated with ocean acidification (21, 22). The long-term warming trend and hyperthermals offer

Significance

From approximately 59 to 51 million years ago, Earth experienced long-term warming during which multiple short-lived global warming events occurred. These events are considered among the best geologic analogs to anthropogenic carbon dioxide release. Here, we use new and published geochemical measurements from Pacific Ocean microfossils that lived 59 to 53 million years ago to calculate atmospheric carbon dioxide and sea surface temperature using a statistical model. We use these results to compute the sensitivity of regional climate to atmospheric CO_2 for long-term warming and the abrupt events. Our findings suggest an influence of plate tectonics on long-term warming and refine constraints on the source and amount of CO_2 released across the multiple timescales of global warming assessed here.

Author contributions: D.T.H., B.H., and J.C.Z. designed research; D.T.H., B.H., and R.E.Z. performed research; D.T.H. and G.J.B. contributed new reagents/analytic tools; D.T.H., B.H., L.L.H., D.E.P., and J.C.Z. analyzed data; and D.T.H., B.H., G.J.B., R.E.Z., L.L.H., D.E.P., and J.C.Z. wrote the paper.

The authors declare no competing interest.

This article is a PNAS Direct Submission.

Copyright © 2024 the Author(s). Published by PNAS. This article is distributed under Creative Commons Attribution-NonCommercial-NoDerivatives License 4.0 (CC BY-NC-ND).

Although PNAS asks authors to adhere to United Nations naming conventions for maps (https://www.un.org/geospatial/mapsgeo), our policy is to publish maps as provided by the authors.

[1]To whom correspondence may be addressed. Email: dustin.t.harper@utah.edu.

This article contains supporting information online at https://www.pnas.org/lookup/suppl/doi:10.1073/pnas.2318779121/-/DCSupplemental.

Published August 26, 2024.

Downloaded from https://www.pnas.org by "UNIVERSITY OF UTAH, MARRIOTT LIBRARY" on August 26, 2024 from IP address 155.98.131.6.

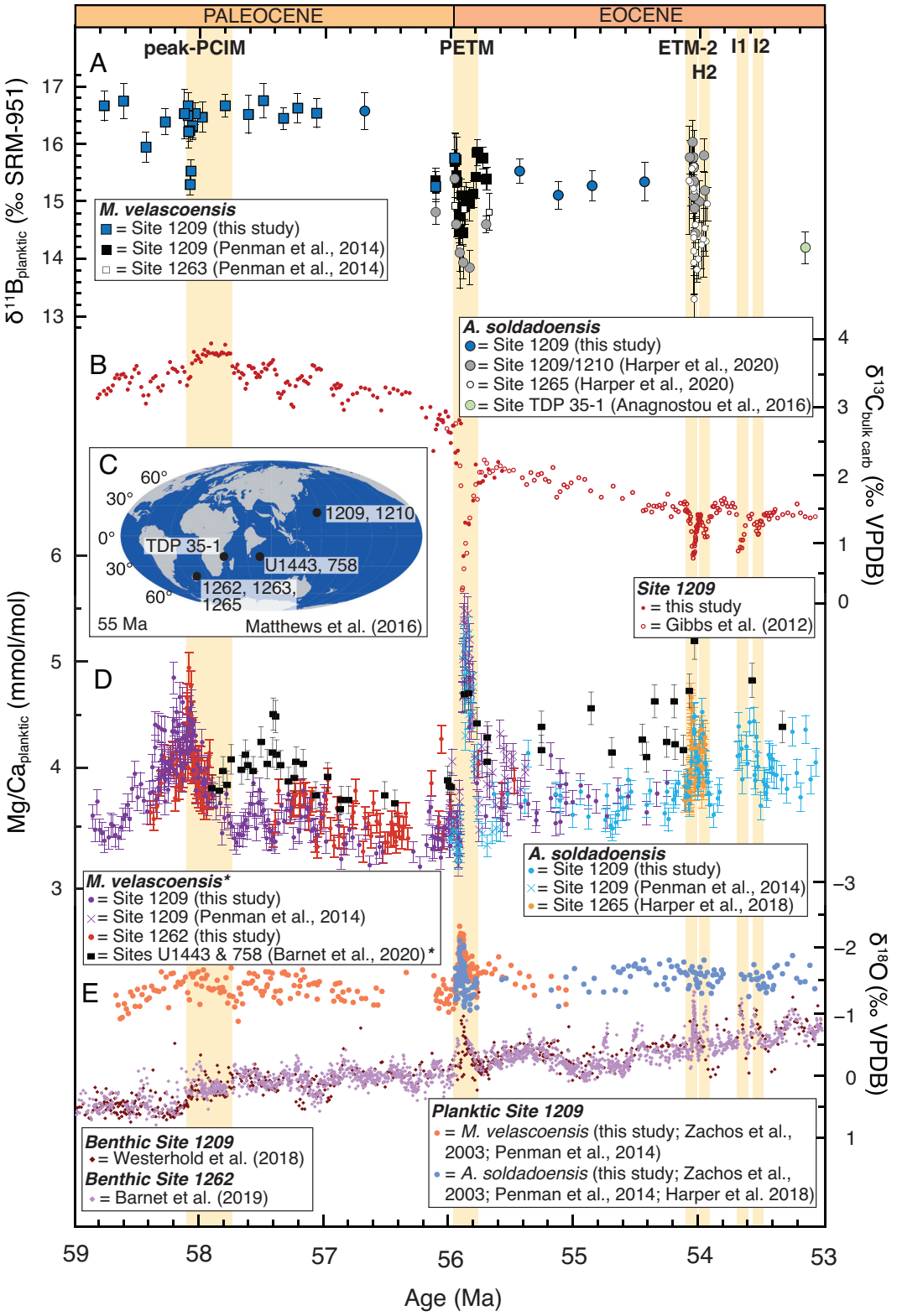

Fig. 1. Compilation of late Paleocene and early Eocene Shatsky Rise (ODP Sites 1209 and 1210), Walvis Ridge (ODP Sites 1262, 1263, and 1265), and Indian Ocean (ODP Site 758 and IODP Site U1443) proxy records. Mixed-layer planktic foraminiferal $\delta^{11}B$ (this study; 6, 7) and the 53.2 Ma Tanzania Drilling Project (TDP) Site 35-1 *Acarinina soldadoensis* $\delta^{11}B$ of Anagnostou et al. (8) (*A*). Bulk carbonate $\delta^{13}C$ (this study; 9) (*B*). Inset map shows 55 Ma paleogeography (10) with site locations (*C*). Mixed-layer planktic foraminiferal Mg/Ca (this study; 6, 11) (*D*). (*) indicates Indian Ocean Mg/Ca compilation includes *Morozovella velascoensis* and *Morozovella subbotinae*, shown to have equivalent Mg/Ca-temperature responses (12). $\delta^{18}O$ benthic (13, 14) and planktic (this study; 6, 11, 15) compilations (*E*). Climate events are highlighted with shaded yellow bars.

opportunities to test the sensitivity of carbon cycle feedbacks and environmental responses to carbon release (e.g., ocean acidification and anoxia, warming, shifts in the hydrologic cycle, changing ecology).

The source of carbon driving LPEE hyperthermals has been debated, with hypothesized mechanisms ranging from North Atlantic Igneous Province (NAIP) volcanism (including thermogenic alteration of organic rich sediments; 23–28) to amplified carbon cycle

Downloaded from https://www.pnas.org by "UNIVERSITY OF UTAH, MARRIOTT LIBRARY" on August 26, 2024 from IP address 155.98.131.6.

feedbacks related to orbital variability (29–32). Despite much research, a consensus has not emerged around a single carbon source or combination of sources during hyperthermals. The magnitude of the carbon isotope excursion (CIE) is one constraint on the mass and source of carbon driving these events (33, 34). However, independent constraints are required to disentangle the respective influence of carbon mass and source on the CIE, as the feasible candidates have $\delta^{13}C$ signatures ranging from −70‰ to −5‰ (e.g., methane- and volcanism-derived CO_2, respectively). Proxies constraining changes in the depth of the CCD (35, 36), ocean acidification (6, 7, 26, 28, 37), and atmospheric CO_2 (38, 39) allow independent assessment of the mass of carbon injected (26, 28, 40, 41). However, while terrestrial CO_2 proxies and CCD-based studies of the PETM suggest relatively small-to-moderate carbon injections (<6,800 gigatons carbon, Gt C) and a moderate to highly ^{13}C-depleted source (38–41), marine foraminiferal boron-based proxy estimates, including boron stable isotopes ($\delta^{11}B$) and B/Ca, suggest moderate to large masses (4,500 to 14,900 Gt C) and require a more ^{13}C-enriched or mixed source (6, 26, 28). Improving the $\delta^{11}B$-based estimates of carbon release (i.e., mass and source) for LPEE hyperthermals requires refining interpretations of uncertainty in $\delta^{11}B$-based records, in particular those from mid-latitude oligotrophic gyre settings which are representative of the global average sea surface acidification response and least likely to be biased by other factors.

Compared with the PETM, drivers of long-term LPEE climate change have received much less attention despite their importance for understanding the background state of the carbon cycle and climate encompassing the hyperthermals and subsequent EECO warmth. Multiple studies have speculated on the role of mantle CO_2 degassing associated with LPEE mid-ocean ridge volcanism (42, 43). Indeed, while the hypothesized main phase of activity occurred close to the Paleocene–Eocene boundary, NAIP volcanism initiated at ~63 Ma and continued into the EECO, potentially contributing to long-term warming (24, 44). In contrast, Komar et al. (21) evaluated carbon cycle model simulations constrained by surface and deep $\delta^{13}C$ and $\delta^{18}O$ values and observations of the CCD, finding that long-term LPEE warming and decline in global $\delta^{13}C$ values were likely driven by a decrease in organic carbon burial over the interval, although they could not rule out contributions from volcanic degassing.

Given the scale of climate change, the LPEE and hyperthermals provide the opportunity to assess Earth climate sensitivity to greenhouse forcing with and without the contribution of other forcing factors, assuming changes in temperature and the carbon cycle can be reasonably well constrained. To this end, we establish 6-Myr records of low- to mid-latitude Pacific sea surface temperature (SST) and paleo-CO_2 for the LPEE [at kiloyears (kyr) to 100s of kyr resolution] using new and previously published planktic foraminiferal proxy data interpreted with a forward proxy system model in a Bayesian hierarchical framework. Proxy system models (45, 46) allow for the interpretation of diverse proxy datasets in the context of wide-ranging modes of environmental change, allowing integration of proxy data with different sampling resolutions and shared sensitivities to environmental parameters while accounting for uncertainties in measurements, proxy calibrations, and secondary (e.g., "vital") effects. Bayesian hierarchical modeling (47) provides a scrupulous way of integrating prior information (e.g., reasonable ranges in environmental variable values for a given time interval) with any relevant data. This allows for more complete and explicit incorporation of assumptions and generates fully interpretable posterior probability distributions of environmental variables, calibrations, and secondary effects.

The model developed here integrates planktic foraminifera Mg/Ca, $\delta^{18}O$ and $\delta^{11}B$ forward proxy system models with an autocorrelated time evolution environmental model (*SI Appendix*). We invert this model to 1) quantify the background state of climate (i.e., North Pacific SST) and the carbon cycle (i.e., atmospheric CO_2) throughout the LPEE, and 2) generate surface ocean pCO_2 estimates, where pCO_2 (in µatm) equals atmospheric CO_2 (or xCO_2, in ppm) at the sea surface, and subtropical North Pacific SST reconstructions for the two largest hyperthermal events (PETM and ETM-2). For the PETM, we inform our interpretations using results from a carbon cycle model simulation (LOSCAR; 48) driven by an emission scenario that matches our CO_2 reconstruction. We discuss long- and short-term carbon cycling and climate sensitivity in the context of CO_2 sources and climate forcing processes implicated by our reconstructions.

Results

Trends in low- to mid-latitude planktic foraminiferal Mg/Ca from the North Pacific (sites 1209 and 1210) and mid-latitude South Atlantic (sites 1262 and 1265) are remarkably similar over the study interval (Fig. 1). Across intervals of overlap, Mg/Ca is largely equivalent between the two species used here, though there are some brief transient interspecies differences in the earliest Eocene (6). Planktic Mg/Ca spikes during warming events and prior to the PCIM with prolonged high Mg/Ca in both the Pacific and Atlantic followed by a decrease coincident with the benthic $\delta^{18}O$ decrease during the peak-PCIM (Fig. 1). Generally, Mg/Ca increases from 59 to 53 Ma, though a period of stability occurs in the late Paleocene from 57.8 to 56 Ma. Raw planktic $\delta^{11}B$ data show previously documented species–species differences that are similar to those observed in modern species (Fig. 1) (7). Overall, North Pacific planktic $\delta^{11}B$ values decrease from the Paleocene to the Eocene (Fig. 1), with large, abrupt decreases prior to the peak-PCIM and during PETM and ETM-2 events (Fig. 1) and relatively stable values between the PETM and ETM-2 (55.6 to 54 Ma).

Reconstructed North Pacific subtropical SST and CO_2, based on the full PSM inversion (*SI Appendix*), both exhibit long-term LPEE trends with sea surface warming of $3.0 \pm \frac{0.4}{0.3}$ °C paralleled by a rise of atmospheric CO_2 from $898 \pm \frac{109}{97}$ to $1{,}686 \pm \frac{447}{342}$ ppm (Fig. 2; all uncertainties are presented as the bounds of the 95% credible interval, or 95% CI). Surface warming of $0.7 \pm \frac{1.0}{1.1}$ °C and a $598 \pm \frac{270}{287}$ ppm increase in CO_2 occurred in the ~500 kyr preceding the PETM (Fig. 2), though the data resolution in this interval makes it difficult to determine the precise timing of this increase. Sea surface cooling of $3.5 \pm \frac{0.5}{0.4}$ °C occurs during the peak-PCIM interval (Fig. 2). Superimposed on the long-term LPEE trend are several transient warming events with magnitudes of $4.0 \pm \frac{0.5}{0.6}$ °C prior to the peak-PCIM, $5.2 \pm \frac{0.4}{0.4}$ °C during the PETM, and $1.9 \pm \frac{0.4}{0.4}$ °C during ETM-2 (Fig. 2). Coeval with each warming event is a positive CO_2 anomaly, with reconstructed increases of $340 \pm \frac{138}{135}$ ppm prior to the peak-PCIM, one doubling (increasing from $1{,}185 \pm \frac{186}{159}$ to $2{,}473 \pm \frac{423}{355}$ ppm) during the PETM, and an increase from $949 \pm \frac{136}{122}$ to $1{,}148 \pm \frac{161}{139}$ ppm during ETM-2 (Fig. 2).

Discussion

Long-Term Carbon Cycling. Reconstructions of the CCD (19, 20), surface and deep ocean $\delta^{13}C$ values (Fig. 1, 9, 13, 14, 49–51), deep ocean warming (49, 50), Tasman gateway sea surface warming (52), and our proxy data (Fig. 2) all indicate a progressive increase in atmospheric CO_2 over the LPEE. Potential C sources contributing

Downloaded from https://www.pnas.org by "UNIVERSITY OF UTAH, MARRIOTT LIBRARY" on August 26, 2024 from IP address 155.98.131.6.

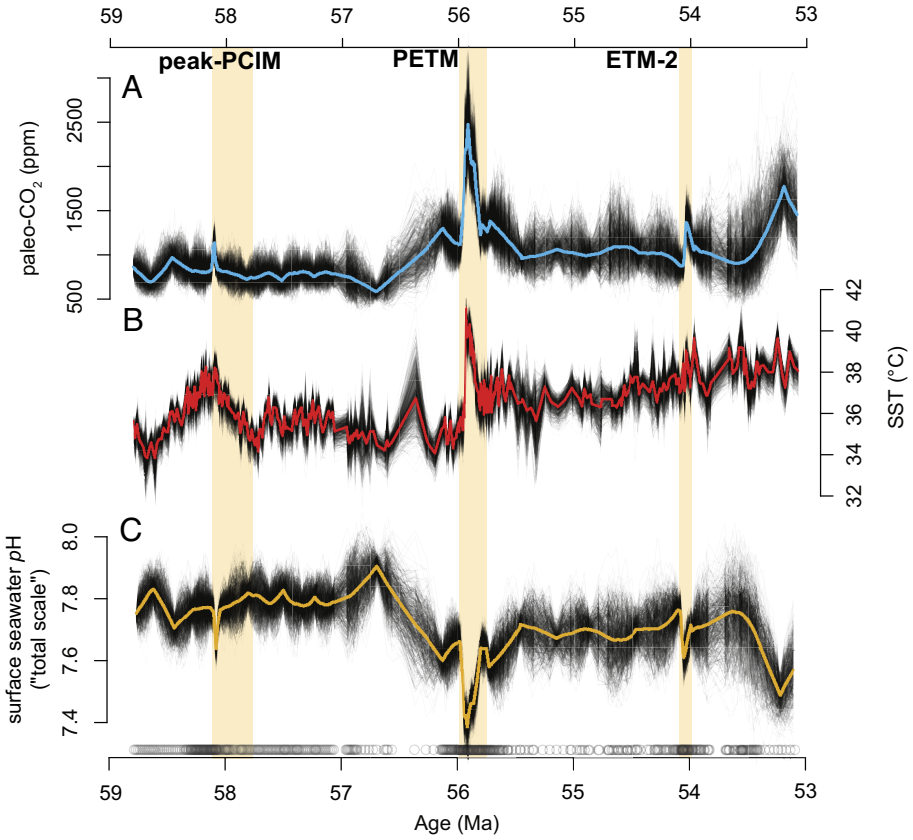

Fig. 2. Forward proxy system model reconstructions of atmospheric CO_2 (*A*), SST (*B*), and surface seawater *p*H (*C*) using Mg/Ca, $\delta^{18}O$, and $\delta^{11}B$ mixed-layer foraminifera data from ODP Sites 1209 and 1210. We include 53.2 Ma Tanzania Drilling Project (TDP) Site 35-1 *A. soldadoensis* $\delta^{11}B$ of Anagnostou et al. (8) to link records and illustrate consistency of the different reconstruction approaches. Grayscale lines are individual draws from 500 time series posteriors, and colored lines show the median of time series posterior distributions. Gray circles along *x* axis indicate model time steps.

to rising atmospheric CO_2 on this timescale include North Atlantic Igneous Province (NAIP) volcanism (e.g., 23, 24, 44), increased organic matter oxidation (i.e., decreasing net burial of organic carbon in sediments; 31, 53), and gradual release of carbon from a gas hydrate capacitor (21). Although carbon cycle modeling studies (21, 53, 54) have demonstrated the plausibility of mechanisms and carbon sources, none of these proposed mechanisms can currently be excluded as a driver of LPEE CO_2 change.

Our reconstruction provides constraints on the magnitude of long-term shifts in carbonate chemistry (e.g., CO_2 increase) over the LPEE, allowing us to evaluate proposed mechanisms of carbon release. Although NAIP volcanism is active over the entire LPEE interval (24, 44), a strictly volcanic carbon source is unlikely given the relatively high $\delta^{13}C$ value of CO_2 emitted from volcanoes, which would require larger carbon emissions to match the observed marine $\delta^{13}C$ values. In particular, Komar et al. (21) found a strictly volcanic carbon source would result in high-magnitude surface ocean acidification and warming. Our results indicate *p*H decrease and SST increase over the LPEE (e.g., Fig. 2), but the magnitude of change we observe is smaller than that required by a strictly volcanic source. Our result does not, however, rule out a contribution of CO_2 derived from thermal volatilization of sedimentary organic carbon in the NAIP region, similar to that proposed for the PETM (25, 27), which could provide more ^{13}C-depleted carbon sources for short periods if not the duration of the LPEE.

Alternatively, marine gas hydrates are highly ^{13}C-depleted and require much smaller emissions to match decreasing $\delta^{13}C$ (34) over the LPEE. We can similarly test this mechanism by comparing carbon cycle model results to our environmental reconstructions. Carbon cycle modeling that includes a dynamic gas hydrate "capacitor" (21), indicates relatively small CO_2 increase (i.e., <350 ppm), surface ocean *p*H decrease (i.e., <0.1) and warming (i.e., <2 °C) because less of the ^{13}C-depleted gas hydrate carbon is required to generate the long-term decrease in ocean $\delta^{13}C$. Therefore, a major role for the hydrate capacitor is inconsistent with the long-term decline in surface *p*H (−0.2) and rise in CO_2 reconstructed here (Fig. 2). Further, carbon emissions from carbon cycle model scenarios with a gas hydrate capacitor mechanism are too small to drive warming equivalent in magnitude to our Pacific SST reconstruction (i.e., $+3.0 \pm \frac{0.4}{0.3}$ °C, this study) and global deep ocean warming >4 °C (49, 50). Thus, proxy-based observations tend to support sources with intermediate $\delta^{13}C$ values (e.g., −25‰ to −20‰) and are consistent with long-term warming driven by a net decrease in the burial of organic matter and/or thermal oxidation of organic matter, but not by long-term release of gas hydrate carbon or strictly volcanic CO_2.

Hyperthermal Events. The major hyperthermals in our reconstructions generally show warming coupled with negative CIEs. One exception is the peak-PCIM (ca. 58.1 to 57.8 Ma; 49; Fig. 1) for which the coupling of the ocean carbon isotope balance and bottom water warming is inverted, with a positive $\delta^{13}C$ excursion (in benthic, planktic, and bulk carbonate; *SI Appendix*, Fig. S1) accompanying benthic warming, mid- to low-latitude sea surface cooling, and following a brief transient rise in CO_2 (Fig. 1). The precise reasons for these proxy responses remain unclear, and understanding the mechanism behind them requires multisite reconstruction of global-scale patterns of environmental change, beyond the scope of this study. The PCIM aside, our collection of ocean carbon chemistry observations can be used to estimate

Downloaded from https://www.pnas.org by "UNIVERSITY OF UTAH, MARRIOTT LIBRARY" on August 26, 2024 from IP address 155.98.131.6.

carbon emissions for the major hyperthermals. In the case of the PETM, Gutjahr et al. (26) estimate a 12,200 Gt C release over the entire duration of the event, requiring a relatively ^{13}C-enriched source (i.e., primarily volcanic degassing). This estimate, however, is based largely on data from a non-gyre location (ODP Site 401) proximal to NAIP and required a much longer carbon release interval (>50 kyr) than is consistent with a wide range of marine and terrestrial observations (e.g., 33). Haynes et al. (28) take a data-driven approach to estimating the mass of carbon released during the PETM using North Pacific Site 1209 data only and likewise suggest massive carbon release (14,900 Gt C) from a relatively ^{13}C-enriched source (δ^{13}C of −10‰).

Our Bayesian reconstructions using data from the oligotrophic North Pacific gyre suggest an increase in atmospheric CO_2 of $+1{,}216 \pm \frac{339}{290}$ ppm (95% CI) from background (Fig. 2), refining the uncertainty in boron-based proxy estimates for the PETM. When these observed changes in atmospheric CO_2 are used in a LOSCAR carbon cycle model simulation, a more modest release of ~5,800 Gt C (4,100 Gt C initial and 1,700 Gt C continuous release) is required (*SI Appendix*, Fig. S7). This mass of carbon, assuming a mean global CIE of −3.5‰ (3), would require a source δ^{13}C of approximately −35‰, consistent with thermogenic methane or a mix of volcanic, organic, and/or methane sources. Therefore, our findings implicate a carbon cycle feedback-driven response to initial warming (e.g., net decreases in organic carbon burial, release of gas hydrate carbon), and/or thermogenic alteration of sediments resulting in volatilization of relatively ^{13}C-depleted carbon mixed with a component of volcanic degassing (i.e., with δ^{13}C ~ −6‰). Although carbon emissions diagnosed from such modeling are subject to further sources of uncertainty that are not explored here, we argue our PETM carbon release estimate is an improvement upon earlier estimates because 1) our Bayesian interpretation of proxy records incorporates all known uncertainties and results in tighter uncertainty bounds on atmospheric CO_2 during the peak-PETM than previous work, and 2) the timing of carbon release in our carbon cycle model scenario (i.e., the majority of release occurring in the first 6 kyr) is most consistent with spatial patterns of carbonate chemistry response (33). For ETM-2, our estimates of warming and atmospheric CO_2 increase (Fig. 2) are consistent with earlier proxy- and model-based results for the event (7), in which mostly organic carbon (i.e., −25‰) is released over 25 kyr, indicating a comparable, albeit slightly less ^{13}C-depleted carbon source for the event compared with the PETM.

Climate Sensitivity. We derive estimates of low- to mid-latitude North Pacific regional climate sensitivity (hereafter referred to as Pacific climate sensitivity, or PCS) on two different timescales, multi-Myr and hyperthermal-scale (kyr to 10s of kyr). Over the 6-Myr study interval, SST increases by $3.0 \pm \frac{0.4}{0.3}$ °C, accompanied by an atmospheric CO_2 increase of $788 \pm \frac{432}{337}$ ppm (Fig. 2), yielding a long-term PCS of $3.5 \pm \frac{2.8}{1.3}$ °C (median with 95% CI) per CO_2 doubling (Fig. 3). This value is smaller than the PCS we estimate for the short-lived PETM and ETM-2 (i.e., $5.3 \pm \frac{2.0}{1.3}$ °C and $5.1 \pm \frac{4.3}{2.3}$ °C per CO_2 doubling, respectively; median with 95% CI; Fig. 3). The difference in PCS over long timescales relative to the short-lived events likely reflects the influence of other boundary conditions, for example, paleogeography, continental weatherability, ocean gateways, and associated ocean circulation changes, on longer-term climate change. This highlights the benefits of focusing on transient CO_2 events to constrain climate sensitivity to CO_2 relevant to modern climate change.

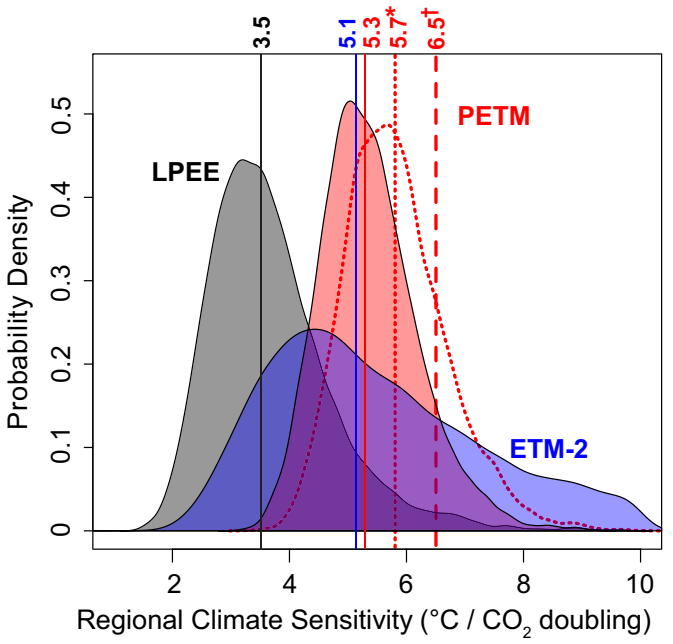

Fig. 3. Regional low- to mid-latitude Pacific Ocean climate sensitivity for the late Paleocene to early Eocene (LPEE; gray; median = 3.5 °C), Paleocene-Eocene Thermal Maximum (PETM; red distribution with median = 5.3 °C), and Eocene Thermal Maximum 2 (ETM-2; blue with median = 5.1 °C) from pre-event and peak-event forward proxy system model posterior distributions of Pacific SST and CO_2. (*) Red dotted distribution and median (5.7 °C) indicate PETM Earth system sensitivity (ESS) calculated using our CO_2 reconstruction and global mean surface temperature (GMST) of Tierney et al. (56). (†) The median PETM ESS of Tierney et al. (56) (red dashed line at 6.5 °C).

Interpretations of hyperthermal-derived sensitivity estimates might also be complicated, however, by changes in other GHG forcings, for example, if direct methane emissions increased atmospheric methane concentrations above background levels as suggested in association with shallow water hydrothermal venting in the NAIP (55).

Our Pacific climate sensitivity for the PETM is slightly lower than ESS calculated by a recent data assimilation study (6.5 °C in Fig. 3; 56), with each study having its relative strengths. The higher data-assimilation-based ESS is due to differences in the approach to calculating paleo-CO_2 and a slightly lower mean temperature change magnitude for our Site 1209 data ($5.2 \pm \frac{0.4}{0.4}$ °C) compared with their global mean surface temperature (GMST) change (cf. 5.6 °C; 56). Although their temperature data assimilation likely better reflect a surface global warming signal because it incorporates the full range in observed warming rather than relying on a single record, Tierney et al. (56) calculated paleo-CO_2 using δ^{11}B from oligotrophic and non-oligotrophic settings (ODP Sites 1209 and 401, respectively). Their cGENIE-based reinterpretation of these records suggests a slightly more modest CO_2 increase (i.e., +900 ppm) than the +1,216 ppm increase reconstructed here (Fig. 2). Moreover, their approach further differs in that they computed *p*H from δ^{11}B using inverse calculation and combined those estimates with carbon cycle model–based estimates of a second carbonate chemistry variable (assuming a fixed increase in Total Alkalinity (TA) from a distribution of pre-PETM TA), to estimate paleo-CO_2 for the PETM. In contrast, our analysis includes uncertainty in the magnitude of dissolved inorganic carbon (DIC) change across the PETM from two different carbon release scenarios and reflects coupling between the boron and carbon systems and other environmental factors like temperature. If we combine our calculated PETM atmospheric CO_2 increase

Downloaded from https://www.pnas.org by "UNIVERSITY OF UTAH, MARRIOTT LIBRARY" on August 26, 2024 from IP address 155.98.131.6.

with the Tierney et al. (56) data assimilation-based estimate of GMST, the resulting ESS of 5.7 $\pm \frac{2.1}{1.3}$ °C per CO_2 doubling is slightly higher than our regional climate sensitivity (i.e., 5.3 $\pm \frac{2.0}{1.3}$ °C; Fig. 3).

Our LPEE PCS also reflects two features in the reconstructions which may be subject to future revision or reinterpretation: 1) the relative stability of reconstructed SST in the latest Paleocene and 2) the long-term *p*H increase from post-PETM recovery to pre-ETM-2 (Figs. 1 and 2) (7). Regarding the first observation, our stable SST estimates contrast with evidence for gradual bottom-water warming (49, 50) and warming in the Tasman gateway (52), but these combined observations may be consistent with the long-term increase in the intensity of meridional ocean overturning evidenced by Neodymium isotope data (57) and also with coarser-resolution Indian Ocean $Mg/Ca_{planktic}$ data (12). These variable warming estimates suggest that additional high-resolution, multiproxy temperature records from well-distributed localities, similar to the PETM study of Dunkley Jones et al. (58), will be needed to more tightly constrain the spatial distribution of warming and assess how the extent to which the pattern of warming observed at our sites represents that of the tropical-subtropical ocean over the late Paleocene. For the second observation, the steady increase in *p*H during the earliest Eocene may be attributable to increases in $\delta^{11}B_{sw}$ values over the interval that are not resolved in our study (7). Here again, high-resolution, multispecies $\delta^{11}B$ studies are needed to reconstruct vertical *p*H gradients and better constrain $\delta^{11}B_{sw}$ change across this interval.

Conclusion

This study provides a long and short timescale assessment of Pacific regional climate sensitivity and forcing mechanisms in the late Paleocene and early Eocene. Although climate forcing processes operating on long and short timescales may differ, warming across both timescales corresponds to CO_2 increase, and carbon sources and/or sinks contributing to carbon cycle change are isotopically comparable on both timescales (i.e., intermediate values of −20‰ to −35‰, though we estimate a more ^{13}C-depleted source mixture for the PETM). Long-term sensitivity to CO_2 forcing is subject to tectonic changes that influence mean global temperature via shifts in ocean circulation and continental weatherability and modulate effects of carbon release. When combined with observations of surface ocean $\delta^{13}C$, our paleo-CO_2 reconstructions are most consistent with intermediate $\delta^{13}C$ source signatures for the PETM and ETM-2 (i.e., −35‰ and −25‰, respectively), indicating a partially or primarily non-volcanic source of carbon (i.e., predominantly thermogenic methane, organic carbon, or a mixture of sources such as NAIP degassing and sedimentary thermogenic volatile release). While not as abrupt as ongoing anthropogenic carbon release, the mass of carbon released during ETM-2 and the PETM falls within future projections of carbon release in IPCC AR6 (i.e., scenarios SSP1-2.6 and SSP3-7.0, respectively; 59). Thus, they provide unique case studies to test carbon cycle feedback mechanisms and sensitivities critical for predicting anthropogenic climate change.

Materials and Methods

ODP Sites 1209 and 1210 were drilled on Leg 198 in the North Pacific at the southern high of the central section of Shatsky Rise. The 55 Ma paleolatitude of both sites is ~28°N, with respective paleodepths of ~1,900 and ~2,100 m for Sites 1209 and 1210 (60, 61). ODP Sites 1262 and 1265 were drilled on Walvis Ridge in the South Atlantic as part of a Paleogene depth transect (Leg 208) and the 55 Ma paleolatitude for these sites is ~42°S (60). Respective paleodepths for Sites 1262 and 1265 are ~3,600 and ~1,850 m (62). Our measurements were augmented by published records from the same locations (6, 7, 9, 11, 13, 14) (Fig. 1). For our interpretation (Fig. 2), we combined Site 1209 and 1210 records and include the earliest (53.2 Ma) *Acarinina soldadoensis* $\delta^{11}B$ of Anagnostou et al. (8) (i.e., mean of 53.2 Ma 250 to 300 and 300 to 355 μm samples from Site TDP 3/5-1 for consistency with our 250 to 355 μm record). We included Site 1262 and 1265 planktic Mg/Ca and benthic $\delta^{18}O$ data (this study; 7, 11, 13) to show the Pacific vs. Atlantic consistency of temperature proxy response. Data are placed on published, orbitally tuned (i.e., to La2010b (63)), consistent age models for each site based on benthic $\delta^{13}C$ (13, 14, 64). Note that these models use the same tuning solution and approach used to develop the age model applied to Indian Ocean Sites 758 and U1443 (12) (Fig. 1).

For the present study, we measured bulk carbonate and mixed-layer planktic foraminiferal (*Morozovella velascoensis* and *A. soldadoensis*; 250 to 355 μm size range) $\delta^{13}C$ and $\delta^{18}O$ via isotope ratio mass spectrometry (IRMS) at ~5 to 25 kyr resolution at UC Santa Cruz. Mg/Ca was measured on homogenized foraminiferal sample splits using an Element XR ICP-MS (inductively coupled plasma mass spectrometer) at UC Santa Cruz following methodology of Harper et al. (7). *M. velascoensis* and *A. soldadoensis* were selected as 1) they are both photosymbiont-bearing constraining them to the photic zone, thus proxy interpretations represent the sea surface, 2) they show an equivalent Mg/Ca response across the PETM (6), and 3) relative differences in their $\delta^{11}B$ vital effects have been documented (7). The use of two species was required as *M. velascoensis* abundances drop to zero in the earliest Eocene. Stable boron isotopes ($\delta^{11}B$) were measured with a Thermo TRITON thermal ionization mass spectrometer in negative mode (N-TIMS) at the Lamont-Doherty Earth Observatory following previously reported approaches (6, 7). The $\delta^{11}B$ compilation used here is lower resolution between climate events (up to ~200 to 400 kyr sampling) than across events (kyr to 10s of kyr). This helps to constrain long-term evolution of CO_2 in these intervals but limits our ability to pick up on short-term CO_2 variability (e.g., orbital scale). Details of analyses are included in *SI Appendix*.

Foraminiferal Mg/Ca and $\delta^{11}B$ have been applied extensively in the Cenozoic over long and short timescales to reconstruct SST and marine carbonate chemistry, respectively. While proxy interpretation is complicated by potential secondary environmental influences (e.g., salinity, major seawater ion concentrations, etc.), recent studies have advanced our understanding of proxy sensitivities to these secondary effects (65–70). We developed a forward proxy system model [PSM; e.g., (45)] in a Bayesian framework following Bowen et al. (71) that uses established relationships [e.g., Hollis et al. (67), Hönisch et al. (72), and references within each] to translate between environmental parameters (e.g., SST and pCO_2) and proxy measurements (Mg/Ca, $\delta^{18}O$ and $\delta^{11}B$). The PSM inversion was accomplished using the rjags (73) and R2jags packages (74) in R version 4.2.1 [R Core, (75)]. Briefly, 1) environmental parameters are modeled as continuous-time, autocorrelated Gaussian variables; parameter values for the timeseries model for each environmental parameter are represented by stochastic terms, with loosely estimated priors based on knowledge of the likely magnitudes of change for each environmental factor; we do not impose any covariance between environmental parameters in the environmental model, 2) the PSM translates the environmental parameter values at any point in time into predicted foraminiferal values ($\delta^{11}B$, $\delta^{18}O$, and Mg/Ca), incorporating uncertainty in various parameters that link environmental and foraminiferal values, 3) the likelihood of the predictions is evaluated against measurements, and 4) the process is repeated using a Markov chain Monte Carlo (MCMC) algorithm to propose subsequent environmental model and PSM parameters and retain model parameter sets in proportion to their likelihood. We ran nine MCMC chains, generating 800,000 posterior samples from each, and evaluated convergence using trace plots, effective sample sizes, and the Gelman–Rubin convergence statistic. Details of the model structure, a complete description of the processes included in the PSM, a suite of sensitivity tests, and statistical assessment of the inversion can be found in *SI Appendix*. The model R codes used in our analysis are provided via Zenodo [10.5281/zenodo.10041865; (76)]. Data used in our analysis and compiled in our figures are provided in *SI Appendix*, Tables S1–S4.

Evans et al. (77) indicate a decline in seawater Mg/Ca (Mg/Ca_{sw}) in the earliest Eocene, though their record does not extend to the late Paleocene. To extend their record, we used coupled benthic Mg/Ca and $\delta^{18}O$ measurements from Site 1209 (50, 78), which indicate declining Mg/Ca_{sw} over the late Paleocene (*SI Appendix*, Fig. S5). Therefore, we assigned broad distributions for [Ca] and [Mg] priors in our

Downloaded from https://www.pnas.org by "UNIVERSITY OF UTAH, MARRIOTT LIBRARY" on August 26, 2024 from IP address 155.98.131.6.

forward model and allowed them to change with time following a conservative estimate of $\Delta Mg/Ca_{sw}$ based on these benthic records for the late Paleocene. These estimates are tied to the early Eocene Mg/Ca_{sw} reconstructions of Evans et al. (77) (see *SI Appendix* for details).

Planktic foraminiferal $\delta^{11}B$ records sea surface *p*H and requires a second carbonate chemistry parameter to compute surface ocean pCO_2 (79). Here, we used DIC and include a sensitivity test in which we use total alkalinity (*SI Appendix*, Fig. S6). Because the structure of our model allows for environmental parameters to change over time according to the likelihood of predicted vs. measured data, but carbon cycle feedbacks are not incorporated into how these parameters change, we prescribe prior DIC distributions for each timestep, which include carbon cycle model- and data-estimated shifts for the second carbonate chemistry parameter, DIC (*SI Appendix*, Fig. S4). Long-term DIC estimates of Zeebe et al. (80) were combined with estimates of ΔDIC for the PETM and ETM-2 (*SI Appendix*, Fig. S3). For the PETM, we used the inverse variance weighted average of DIC change from 1) the most massive emission scenario (14,900 Gt C) derived from planktic B/Ca [(28); *SI Appendix*, Fig. S3] and 2) the mean of two conservative emission scenarios using the LOSCAR carbon cycle model [see Zeebe (48) for model description] in which 3,000 to 4,500 Gt C is released (this study; *SI Appendix*, Fig. S3). We set model-derived 2σ DIC uncertainty to 0.3 mmol/kg. Thus, for the PETM, uncertainty in model-derived DIC is much larger than the range represented by our LOSCAR emission scenarios (i.e., maximum of ±0.06 mmol/kg; *SI Appendix*, Fig. S3). 2σ uncertainty in ΔDIC for the PETM spans the response range of other carbon cycle model simulations including the cGENIE volcanic emission scenario of Gutjahr et al. (26). For ETM-2, mean values for prior DIC distributions are defined by the mean of two different LOSCAR carbon release scenarios (this study; *SI Appendix*, Fig. S3) and prescribed 0.3 mmol/kg 2σ uncertainty. For the entire study interval (i.e., including non-hyperthermal intervals), we set DIC prior distribution 2σ to 0.3 mmol/kg for any time steps for which our DIC prior $2\sigma < 0.3$ mmol/kg (*SI Appendix*, Fig. S4).

The LOSCAR carbon cycle box model was used to determine the mass and $\delta^{13}C$ of carbon released during the PETM (*SI Appendix*). Briefly, a carbon emission scenario was tailored so that LOSCAR-based calculations of atmospheric CO_2 aligned with our proxy model reconstruction (*SI Appendix*, Fig. S7*B*). This was accomplished with an initial 6-kyr release of 4,100 Gt C with an isotopic composition of −35‰ followed by a 140-kyr slow leak of 1,700 Gt C with the same isotopic composition (*SI Appendix*, Fig. S7). Our LOSCAR model run includes temperature-dependent remineralization of organic carbon following Zeebe (81).

We calculate regional climate sensitivity using our SST and atmospheric CO_2 posterior distributions, averaged across pre-event baseline intervals and peak-event intervals. For hyperthermals, the pre-event baselines include time steps that correspond to pre-CIE ages and have sustained SSTs (±<0.5 °C), and peak-event intervals include time steps that correspond to the highest sustained temperatures within the main body CIE. For the PETM, the pre-event baseline is 56.120 to 55.965 Ma with peak-event 55.905 to 55.894 Ma. For ETM-2, the baseline is 54.100 to 54.085 Ma with peak-event 53.995 to 53.950 Ma. Long-term regional climate sensitivity is calculated using our SST and atmospheric CO_2 posterior distributions, averaged across 58.800 to 58.300 Ma and 53.250 to 53.000 Ma. These intervals were selected as they are likely to represent a mean climate state (i.e., averaged over 100 s of kyr with relatively stable SSTs of ±<1.5 °C).

Data, Materials, and Software Availability. Analytical data, statistical model code and statistical model output data have been deposited in Zenodo (76) (DOI: 10.5281/zenodo.10041865). All analytical data and carbon cycle model output data are included in the manuscript and/or supporting information.

ACKNOWLEDGMENTS. We thank Rob Franks, Dyke Andreasen, and Colin Carney for their technical support. Discussions with Eleni Anagnostou, Oscar Branson, and Michael Henehan helped improve data interpretation. Thank you to the editor John Valley, and to Jessica Tierney and two anonymous reviewers for providing feedback which improved this work. Thank you to the CO_2 Proxy Integration Project (CO_2PIP; paleo-co2.org) community for their feedback and support of this work. This research used samples provided by the International Ocean Discovery Program (IODP) and legacy programs (i.e., ODP), and was funded by NSF Awards OCE 1658017 to J.C.Z.; OCE 1657848 to B.H.; OCE-2001022 and OCE-2034660 to R.E.Z.; OCE-2202983 to D.E.P.; and EAR-2121170 to G.J.B.

Author affiliations: [a]Department of Geology and Geophysics, University of Utah, Salt Lake City, UT 84112; [b]Department of Earth and Environmental Sciences and Lamont-Doherty Earth Observatory of Columbia University, Palisades, NY 10964; [c]School of Ocean and Earth Science and Technology, Department of Oceanography, University of Hawaii at Manoa, Honolulu, HI 96822; [d]Department of Earth Science and Geography, Vassar College, Poughkeepsie, NY 12604; [e]Department of Geosciences, Utah State University, Logan, UT 84321; and [f]Department of Earth and Planetary Sciences, University of California, Santa Cruz, CA 95064

1. D. L. Royer, "Atmospheric CO_2 and O_2 during the Phanerozoic: Tools, patterns, and impacts" in *Treatise on Geochemistry (Second Edition)*, J. Farquhar, Ed. (Elsevier, Amsterdam, 2014), vol. 6.
2. K. G. Miller, T. R. Janecek, M. E. Katz, D. J. Keil, Abyssal circulation and benthic foraminiferal changes near the Paleocene/Eocene boundary. *Paleoceanography* **2**, 20 (1987).
3. H. McCarren, E. Thomas, T. Hasegawa, U. Röhl, J. C. Zachos, Depth dependency of the Paleocene-Eocene carbon isotope excursion: Paired benthic and terrestrial biomarker records (Ocean Drilling Program Leg 208, Walvis Ridge). *Geochem., Geophys., Geosyst.* **9**, Q10008 (2008).
4. M. J. Cramwinckel *et al.*, Synchronous tropical and polar temperature evolution in the Eocene. *Nature* **559**, 382–386 (2018).
5. E. Anagnostou *et al.*, Proxy evidence for state-dependence of climate sensitivity in the Eocene greenhouse. *Nat. Commun.* **11**, 4436 (2020).
6. D. E. Penman, B. Hönisch, R. E. Zeebe, E. Thomas, J. C. Zachos, Rapid and sustained surface ocean acidification during the Paleocene-Eocene Thermal Maximum. *Paleoceanography* **29**, 357–369 (2014).
7. D. T. Harper *et al.*, The magnitude of surface ocean acidification and carbon release during Eocene Thermal Maximum 2 (ETM-2) and the Paleocene-Eocene Thermal Maximum (PETM). *Paleoceanogr. Paleoclimatol.* **35**, e2019PA003699 (2020).
8. E. Anagnostou *et al.*, Changing atmospheric CO_2 concentration was the primary driver of early Cenozoic climate. *Nature* **533**, 380–384 (2016).
9. S. J. Gibbs *et al.*, Scaled biotic disruption during early Eocene global warming events. *Biogeosciences* **9**, 4679–4688 (2012).
10. K. J. Matthews *et al.*, Global plate boundary evolution and kinematics since the late Paleozoic. *Global Planet. Change* **146**, 226–250 (2016).
11. D. T. Harper *et al.*, Subtropical sea-surface warming and increased salinity during Eocene Thermal Maximum 2. *Geology* **46**, 187–190 (2018).
12. J. S. K. Barnet *et al.*, Coupled evolution of temperature and carbonate chemistry during the Paleocene-Eocene; new trace element records from the low latitude Indian Ocean. *Earth Planet. Sci. Lett.* **545**, 116414 (2020).
13. J. S. K. Barnet *et al.*, A high-fidelity Benthic stable isotope record of late Cretaceous-early Eocene climate change and carbon-cycling. *Paleoceanogr. Paleoclimatol.* **34**, 672–691 (2019).
14. T. Westerhold, U. Röhl, B. Donner, J. C. Zachos, Global extent of early Eocene hyperthermal events: A new Pacific Benthic foraminiferal isotope record from Shatsky Rise (ODP Site 1209). *Paleoceanogr. Paleoclimatol.* **33**, 626–642 (2018).
15. J. C. Zachos *et al.*, A transient rise in tropical sea surface temperature during the Paleocene-Eocene Thermal Maximum. *Science* **302**, 1551–1554 (2003).
16. The Cenozoic CO_2 Proxy Integration Project (CENCO2PIP) Consortium *et al.*, Toward a Cenozoic history of atmospheric CO_2. *Science* **382**, eadi5177 (2023).
17. J. W. B. Rae *et al.*, Atmospheric CO_2 over the past 66 million years from marine archives. *Annu. Rev. Earth Planet. Sci.* **49**, 609–641 (2021).
18. T. Westerhold *et al.*, An astronomically dated record of Earth's climate and its predictability over the last 66 million years. *Science* **369**, 5 (2020).
19. H. J. L. Hancock, G. R. Dickens, E. Thomas, K. L. Blake, Reappraisal of early Paleogene CCD curves: Foraminiferal assemblages and stable carbon isotopes across the carbonate facies of Perth Abyssal Plain. *Int. J. Earth Sci.* **96**, 925–946 (2007).
20. B. S. Slotnick *et al.*, Early Paleogene variations in the calcite compensation depth: New constraints using old borehole sediments from across Ninetyeast Ridge, central Indian Ocean. *Clim. Past* **11**, 473–493 (2015).
21. N. Komar, R. E. Zeebe, G. R. Dickens, Understanding long-term carbon cycle trends: The late Paleocene through the early Eocene. *Paleoceanography* **28**, 650–662 (2013).
22. D. E. Penman *et al.*, An abyssal carbonate compensation depth overshoot in the aftermath of the Palaeocene-Eocene Thermal Maximum. *Nat. Geosci.* **9**, 575–580 (2016).
23. H. Svensen *et al.*, Release of methane from a volcanic basin as a mechanism for intial Eocene global warming. *Nature* **429**, 4 (2004).
24. M. Storey, R. A. Duncan, C. Tegner, Timing and duration of volcanism in the North Atlantic Igneous Province: Implications for geodynamics and links to the Iceland hotspot. *Chem. Geol.* **241**, 264–281 (2007).
25. J. Frieling *et al.*, Thermogenic methane release as a cause for the long duration of the PETM. *Proc. Natl. Acad. Sci. U.S.A.* **113**, 12059–12064 (2016).
26. M. Gutjahr *et al.*, Very large release of mostly volcanic carbon during the Palaeocene-Eocene Thermal Maximum. *Nature* **548**, 573–577 (2017).
27. S. M. Jones, M. Hoggett, S. E. Greene, T. Dunkley Jones, Large Igneous Province thermogenic greenhouse gas flux could have initiated Paleocene-Eocene Thermal Maximum climate change. *Nat. Commun.* **10**, 5547 (2019).
28. L. L. Haynes, B. Hönisch, The seawater carbon inventory at the Paleocene-Eocene Thermal Maximum. *Proc. Natl. Acad. Sci. U.S.A.* **117**, 24088–24095 (2020).
29. L. J. Lourens *et al.*, Astronomical pacing of late Palaeocene to early Eocene global warming events. *Nature* **435**, 1083–1087 (2005).
30. R. Zeebe, L. Lourens, Solar System chaos and the Paleocene-Eocene boundary age constrained by geology and astronomy. *Science* **365**, 4 (2019).
31. R. M. DeConto *et al.*, Past extreme warming events linked to massive carbon release from thawing permafrost. *Nature* **484**, 87–91 (2012).

Downloaded from https://www.pnas.org by "UNIVERSITY OF UTAH, MARRIOTT LIBRARY" on August 26, 2024 from IP address 155.98.131.6.

32. G. J. Bowen, Up in smoke: A role for organic carbon feedbacks in Paleogene hyperthermals. *Global Planet. Change* **109**, 18–29 (2013).
33. S. Kirtland Turner, A. Ridgwell, Development of a novel empirical framework for interpreting geological carbon isotope excursions, with implications for the rate of carbon injection across the PETM. *Earth Planet. Sci. Lett.* **435**, 1–13 (2016).
34. F. A. McInerney, S. L. Wing, The Paleocene-Eocene Thermal Maximum: A perturbation of carbon cycle, climate, and biosphere with implications for the future. *Annu. Rev. Earth Planet. Sci.* **39**, 489–516 (2011).
35. J. C. Zachos *et al.*, Rapid acidification of the ocean during the Paleocene-Eocene Thermal Maximum. *Science* **308**, 1611–1615 (2005).
36. A. B. Colosimo, T. J. Bralower, J. C. Zachos, "Evidence for lysocline shoaling at the Paleocene/Eocene Thermal Maximum on Shatsky Rise, Northwest Pacific" in *Proceedings of the Ocean Drilling Program Scientific Results* (2006), vol. 198.
37. T. L. Babila *et al.*, Capturing the global signature of surface ocean acidification during the Palaeocene-Eocene Thermal Maximum. *Philos. Trans. A, Math. Phys. Eng. Sci.* **376**, 20170072 (2018).
38. Y. Cui, B. A. Schubert, Atmospheric pCO_2 reconstructed across five early Eocene global warming events. *Earth Planet. Sci. Lett.* **478**, 225–233 (2017).
39. G. J. Bowen *et al.*, Two massive, rapid releases of carbon during the onset of the Palaeocene–Eocene thermal maximum. *Nat. Geosci.* **8**, 44–47 (2014).
40. K. Panchuk, A. Ridgwell, L. R. Kump, Sedimentary response to Paleocene-Eocene Thermal Maximum carbon release: A model-data comparison. *Geology* **36**, 315–318 (2008).
41. R. E. Zeebe, J. C. Zachos, G. R. Dickens, Carbon dioxide forcing alone insufficient to explain Palaeocene-Eocene Thermal Maximum warming. *Nat. Geosci.* **2**, 576–580 (2009).
42. R. M. Owen, D. K. Rea, Sea-floor hydrothermal activity links climate to tectonics: The Eocene carbon dioxided greenhouse. *Science* **227**, 3 (1985).
43. O. Eldholm, E. Thomas, Environmental impacts of volcanic margin formation. *Earth Planet. Sci. Lett.* **117**, 10 (1993).
44. C. M. Wilkinson, M. Ganerød, B. W. H. Hendriks, E. A. Eide, Compilation and appraisal of geochronological data from the North Atlantic Igneous Province (NAIP). *Geol. Soc., London, Spec. Publ.* **447**, 69–103 (2017).
45. M. N. Evans, S. E. Tolwinski-Ward, D. M. Thompson, K. J. Anchukaitis, Applications of proxy system modeling in high resolution paleoclimatology. *Q. Sci. Rev.* **76**, 16–28 (2013).
46. S. Dee *et al.*, PRYSM: An open-source framework for PRoxY System Modeling, with applications to oxygen-isotope systems. *J. Adv. Model. Earth Syst.* **7**, 1220–1247 (2015).
47. M. P. Tingley *et al.*, Piecing together the past: Statistical insights into paleoclimatic reconstructions. *Q. Sci. Rev.* **35**, 1–22 (2012).
48. R. E. Zeebe, LOSCAR: Long-term Ocean-atmosphere-Sediment CArbon cycle Reservoir model v2.0.4. *Geosci. Model Dev.* **5**, 149–166 (2012).
49. K. Littler, U. Röhl, T. Westerhold, J. C. Zachos, A high-resolution benthic stable-isotope record for the South Atlantic: Implications for orbital-scale changes in Late Paleocene–Early Eocene climate and carbon cycling. *Earth Planet. Sci. Lett.* **401**, 18–30 (2014).
50. T. Westerhold, U. Röhl, B. Donner, H. K. McCarren, J. C. Zachos, A complete high-resolution Paleocene benthic stable isotope record for the central Pacific (ODP Site 1209). *Paleoceanography* **26**, PA2216 (2011).
51. S. Setty *et al.*, Loss of Earth system resilience during early Eocene transient global warming events. *Sci. Adv.* **9**, 10 (2023).
52. P. K. Bijl *et al.*, Early Palaeogene temperature evolution of the southwest Pacific Ocean. *Nature* **461**, 776–779 (2009).
53. A. C. Kurtz, L. R. Kump, M. A. Arthur, J. C. Zachos, A. Paytan, Early Cenozoic decoupling of the global carbon and sulfur cycles. *Paleoceanography* **18**, 1090 (2003).
54. A. K. Hilting, L. R. Kump, T. J. Bralower, Variations in the oceanic vertical carbon isotope gradient and their implications for the Paleocene-Eocene biological pump. *Paleoceanography* **23**, PA3222 (2008).
55. C. Berndt *et al.*, Shallow-water hydrothermal venting linked to the Palaeocene–Eocene Thermal Maximum. *Nat. Geosci.* **16**, 803–809 (2023).
56. J. E. Tierney *et al.*, Spatial patterns of climate change across the Paleocene-Eocene Thermal Maximum. *Proc. Natl. Acad. Sci. U.S.A.* **119**, e2205326119 (2022).
57. S. J. Batenburg *et al.*, Major intensification of Atlantic overturning circulation at the onset of Paleogene greenhouse warmth. *Nat. Commun.* **9**, 4954 (2018).
58. T. Dunkley Jones *et al.*, Climate model and proxy data constraints on ocean warming across the Paleocene–Eocene Thermal Maximum. *Earth-Sci. Rev.* **125**, 123–145 (2013).
59. IPCC, "Climate change 2022: Impacts, adaptation and vulnerability" in *Contribution of Working Group II to the Sixth Assessment Report of the Intergovernmental Panel on Climate Change*, H.-O. Pörtner *et al.*, Eds. (Cambridge, UK/New York, NY, 2022), p. 3056.
60. D. J. van Hinsbergen *et al.*, A Paleolatitude Calculator for Paleoclimate studies. *PLoS ONE* **10**, e0126946 (2015).
61. K. Takeda, K. Kaiho, Faunal turnovers in central Pacific benthic foraminifera during the Paleocene-Eocene Thermal Maximum. *Palaeogeogr. Palaeoclimatol. Palaeoecol.* **251**, 175–197 (2007).
62. J. C. Zachos *et al.*, "Initial reports. Early cenozoic extreme climates: The walvis ridge transect" in *Proceedings of the Ocean Drilling Program* (2004), vol. 208.
63. J. Laskar, A. Fienga, M. Gastineau, H. Manche, La2010: a new orbital solution for the long-term motion of the Earth. *Astron. Astrophys.*, **532**, A89 (2011).
64. T. Westerhold *et al.*, Astronomical calibration of the Ypresian timescale: Implications for seafloor spreading rates and the chaotic behavior of the solar system? *Clim. Past* **13**, 1129–1152 (2017).
65. L. L. Haynes, B. Hönisch, K. Holland, S. Eggins, Y. Rosenthal, Calibrating non-thermal effects on planktic foraminiferal Mg/Ca for application across the Cenozoic. *Paleoceanogr. Paleoclimatol.* **38**, e2023PA004613 (2023).
66. K. Holland *et al.*, Constraining multiple controls on planktic foraminifera Mg/Ca. *Geochim. Cosmochim. Acta* **273**, 116–136 (2020).
67. C. J. Hollis *et al.*, The DeepMIP contribution to PMIP4: methodologies for selection, compilation and analysis of latest Paleocene and early Eocene climate proxy data, incorporating version 0.1 of the DeepMIP database. *Geosci. Model. Dev.* **12**, 3149–3206 (2019).
68. M. J. Henehan *et al.*, A new boron isotope-pH calibration for *Orbulina universa*, with implications for understanding and accounting for 'vital effects'. *Earth Planet. Sci. Lett.* **454**, 282–292 (2016).
69. G. L. Foster, J. W. B. Rae, Reconstructing ocean pH with boron isotopes in *Foraminifera*. *Annu. Rev. Earth Planet. Sci.* **44**, 207–237 (2016).
70. B. Hönisch *et al.*, The influence of salinity on Mg/Ca in planktic foraminifers–Evidence from cultures, core-top sediments and complementary δ18O. *Geochim. Cosmochim. Acta* **121**, 196–213 (2013).
71. G. J. Bowen, B. Fischer-Femal, G.-J. Reichart, A. Sluijs, C. H. Lear, Joint inversion of proxy system models to reconstruct paleoenvironmental time series from heterogeneous data. *Clim. Past* **16**, 65–78 (2020).
72. B. r. Hönisch *et al.*, *Boron Proxies in Paleoceanography and Paleoclimatology* (John Wiley & Sons Ltd., 2019).
73. M. Plummer, rjags: Bayesian graphical models using MCMC. (CRAN) R package (version 4–15, CRAN, 2018).
74. Y.-S. Su, M. Yajima, R2jags: Using R to Run 'JAGS'. (CRAN) R package (version 0.8-5, CRAN, 2015).
75. R. C. Team, *R: A Language and Environment for Statistical Computing* (R Foundation for Statistical Computing, Vienna, Austria, 2022).
76. D. T. Harper, G. J. Bowen, SPATIAL-Lab/boron: Harper et al. (2024) PNAS code, output and data (v1.0). Zenodo. https://doi.org/10.5281/zenodo.10041865. Deposited 23 July 2024.
77. D. Evans *et al.*, Eocene greenhouse climate revealed by coupled clumped isotope-Mg/Ca thermometry. *Proc. Natl. Acad. Sci. U.S.A.* **115**, 1174–1179 (2018).
78. A. Dutton, K. C. Lohmann, R. M. Leckie, Insights from the Paleogene tropical Pacific: Foraminiferal stable isotope and elemental results from Site 1209, Shatsky Rise. *Paleoceanography* **20**, 16 (2005).
79. R. E. Zeebe, D. Wolf-Gladrow, "CO_2 in seawater: Equilibrium, kinetics, isotopes" in *Elsevier Oceanography Series*, D. Halpern, Ed. (Elsevier Science B.V., 2001), vol. 65.
80. R. E. Zeebe, T. Tyrrell, History of carbonate ion concentration over the last 100 million years II: Revised calculations and new data. *Geochim. Cosmochim. Acta* **257**, 373–392 (2019).
81. R. E. Zeebe, What caused the long duration of the Paleocene-Eocene Thermal Maximum? *Paleoceanography* **28**, 440–452 (2013).

Downloaded from https://www.pnas.org by "UNIVERSITY OF UTAH, MARRIOTT LIBRARY" on August 26, 2024 from IP address 155.98.131.6.